inorganics

MDPI

Article

A Graphene Oxide-Angiogenin Theranostic Nanoplatform for the Therapeutic Targeting of Angiogenic Processes: The Effect of Copper-Supplemented Medium

Lorenzo Riela [1], Lorena Maria Cucci [1], Örjan Hansson [2], Tiziano Marzo [3,4], Diego La Mendola [3,4] and Cristina Satriano [1,4,*]

[1] Department of Chemical Sciences, University of Catania, Viale A. Doria, 6, 95125 Catania, Italy
[2] Department of Chemistry and Molecular Biology, University of Gothenburg, SE-40530 Göteborg, Sweden
[3] Department of Pharmacy, University of Pisa, Via Bonanno Pisano 6, 56126 Pisa, Italy
[4] Consorzio Interuniversitario di Ricerca in Chimica dei Metalli nei Sistemi Biologici (C.I.R.C.M.S.B.), viale C. Ulpiani 27, 70126 Bari, Italy
* Correspondence: cristina.satriano@unict.it

Abstract: Graphene oxide (GO) nanosheets with different content in the defective carbon species bound to oxygen sp3 were functionalized with the angiogenin (ANG) protein, to create a novel nanomedicine for modulating angiogenic processes in cancer therapies. The GO@ANG nanocomposite was scrutinized utilizing UV-visible and fluorescence spectroscopies. GO exhibits pro- or antiangiogenic effects, mostly attributed to the disturbance of ROS concentration, depending both on the total concentration (i.e., >100 ng/mL) as well as on the number of carbon species oxidized, that is, the C/O ratio. ANG is considered one of the most effective angiogenic factors that plays a vital role in the angiogenic process, often in a synergic role with copper ions. Based on these starting hypotheses, the GO@ANG nanotoxicity was assessed with the MTT colorimetric assay, both in the absence and in the presence of copper ions, by in vitro cellular experiments on human prostatic cancer cells (PC-3 line). Laser confocal microscopy (LSM) cell imaging evidenced an enhanced internationalization of GO@ANG than bare GO nanosheets, as well as significant changes in cell cytoskeleton organization and mitochondrial staining compared to the cell treatments with free ANG.

Keywords: 2D nanomaterials; base-washed graphene oxide; PC-3 cells; nanotoxicity; confocal microscopy; cell cytoskeleton; ROS; copper

Citation: Riela, L.; Cucci, L.M.; Hansson, Ö.; Marzo, T.; La Mendola, D.; Satriano, C. A Graphene Oxide-Angiogenin Theranostic Nanoplatform for the Therapeutic Targeting of Angiogenic Processes: The Effect of Copper-Supplemented Medium. *Inorganics* **2022**, *10*, 188. https://doi.org/10.3390/inorganics10110188

Academic Editors: Snezana Jovanovic-Stevic, Tanja Soldatovic and Ralph Puchta

Received: 24 September 2022
Accepted: 26 October 2022
Published: 29 October 2022

1. Introduction

Angiogenesis is the physiological process by which new blood vessels are formed from pre-existing ones, and occurs throughout life in both health and disease [1]. The general balance of pro- and antiangiogenic signals within the human body regulates normal angiogenesis. In disease conditions, the goal of therapeutic targeting of the angiogenic process is to normalize vasculature in target tissues by enhancing angiogenesis, where reduced vascularity and blood flow occur, such as in tissue ischemia and wound repair; or to inhibit angiogenesis, as in the case of excessive and abnormal angiogenesis originating from cancer [2].

Nanomaterials have captured attention recently as angiogenesis modulators. For example, gold nanoparticles reduce the viability, migration, and tube formation of endothelial cells [3–5] and have been shown to affect the activity of vascular endothelial growth factor (VEGF) and basic fibroblast growth factor (bFGF) [6]. Similarly, silver nanoparticles have been reported to inhibit VEGF-induced cell proliferation, migration, and tube formation. Functionalization of gold and silver nanoparticles with peptides or proteins can improve both activity and selectivity in the tuning of angiogenesis [7–10].

Two-dimensional nanomaterials have also drawn attention for their application as a novel nanomedicine platform, due to their high loading capacity and remarkable physicochemical and biological properties [11]. Specifically, graphene-based nanomaterials have been found to have great potential to modulate angiogenesis [12]. Intracellular formation of reactive oxygen species (ROS) and nitrogen species (NOS), as well as activation of phospho-eNOS and phospho-Akt, are plausible mechanisms for angiogenesis induced by graphene oxide (GO) and reduced GO (rGO) [13,14]. Examples of applications include electroactive patches of single-layer GO-incorporated collagen assisting vascularization for cardiac tissue engineering [15]; GO/polycaprolactone nanoscaffolds promoting angiogenesis in peripheral nerve regeneration through the Akt-eNOS-VEGF signaling pathway [16]; and rGO-incorporated hydrogel promoting angiogenesis for wound-healing applications [17].

In addition to proangiogenic activity and wound-healing potential, the most recent applications of GO in angiogenesis include antiangiogenic activity, and therapeutic (anticancer activity, drug/gene delivery, photothermal/immunotherapy) and bioimaging applications for various cancer diseases [18–22]. It should be noted that GO/rGO can promote angiogenesis at low concentration (<100 ng) [23]. However, an antiangiogenic effect has also been demonstrated at a concentration greater than 100 ng, attributed to the excessive generation of intracellular ROS [13,24]. In general, the mechanisms underlying GO toxicity, in addition to oxidative stress and excessive ROS production, also include DNA damage, apoptosis, autophagy, and immune responses, which vary widely regarding the physicochemical properties of GO, such as surface chemistry, lateral size, and purity [25–27].

Alongside the conventional definition of GO structure, i.e., differently large carbon sp^2 domains interrupted by sp^3 carbon atoms containing oxygen-based hydrophilic functionalities, such as hydroxyl, epoxydic, and carboxylic functional groups [5], GO also comprises one additional component called oxidative debris (OD), small and highly oxidized fragments adsorbed on the GO surface [28].

In the present work, we scrutinize GO in two different C/O ratios, namely, GO after removal of OD using an alkaline washing process [29] (base-washed GO, hereafter referred to as bwGO); and the as-received GO ultrasonicated for two hours to obtain a homogeneous dispersion of approximately 200 nm in lateral size [27] (hereafter named GO120s) in their assembly with angiogenin protein (ANG), in the absence or presence of copper ions.

ANG is a ubiquitous protein with a strong angiogenic effect, able to stimulate new vessel growth and cell self-renewal under physiological conditions such as neuroprotection [30], inflammation [31], and immune response [32]. The protein–protein interaction in which ANG is involved triggers several signal pathways [33], by increasing the production of ribosomal proteins and enhancing the growth and proliferation of endothelial cells involved in neurodegenerative disorders such as amyotrophic lateral sclerosis (ALS) [34], Parkinson's disease (PD), and Crohn's disease (CrD) [35]. A critical role of ANG in angiogenesis is further demonstrated by evidence that up-regulation of the protein is evident in different types of tumors, including lymphoma, melanoma, breast, cervical, colon, liver, prostate, and kidney cancers. Therefore, ANG may serve as a therapeutic target for drug development in the treatment of cancer based on angiogenin-stimulated angiogenesis and cancer cell proliferation [36].

Copper regulates ANG expression and modulates its activity by forming metal protein assemblies [37,38]. Copper ions bind to the catalytic site of ANG [39], whilst data have proved that the presence of Cu^{2+} enhances the number of ANG molecules bound to endothelial cells [40]. Furthermore, copper acts as a cofactor of many metalloenzymes and is essential for iron homeostasis, involving the participation of copper in blood coagulation processes and angiogenesis [41,42].

The role of copper in angiogenesis is also demonstrated by its ability to stimulate endothelial cell migration [43], while increased serum levels of copper have been detected in patients with different types of tumors and related to tumor onset and progression [44,45]. We recently demonstrated that a hybrid nanoplatform of gold nanoparticles and S28CANG, an ANG mutant with cysteine instead of serine at residue 28 of the protein, could modulate

the angiogenesis process involved in wound-healing by the combined actions of nanogold (antiangiogenic and anti-inflammatory) and protein (proangiogenic) on endothelial cells [7].

In this work, a new ANG-GO nanohybrid was prepared by assembling GO with a fluorescent derivative of ANG, namely ANGF488, obtained by conjugating the primary amines of the protein with the reactive dye Alexa fluor 488 tetrafluorphenyl (TFP). The physicochemical characterization to confirm the effective immobilization of the protein by physisorption on bwGO and GO120s nanosheets was carried out by optical spectroscopy (UV-visible and fluorescence). The theranostic capacity of the ANG-GO nanohybrid was tested on prostate cancer cells (PC-3 line), in the presence or absence of copper ions, by the MTT assay and laser-scanning confocal microscopy (LSM) analyzes, to assess nanotoxicity and analyze by cell imaging the perturbation induced on cell cytoskeleton and intracellular organelles, respectively.

2. Results

2.1. UV-Visible and Fluorescence Spectra Analysis

UV-vis spectra collected for the two GO nanoplatforms, before and after the functionalization with the fluorescent ANG, are reported in Figure 1. The spectrum of the free protein, ANGAF488, is also included for comparison.

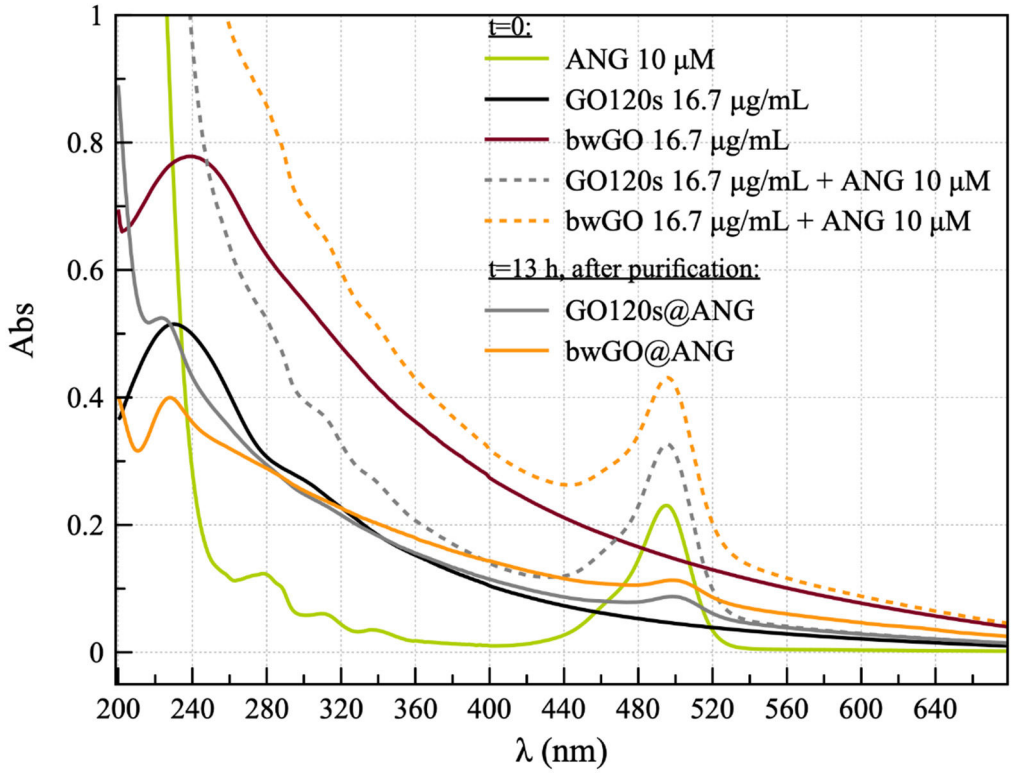

Figure 1. UV-vis spectra for the ANGAF488 protein (green solid line); GO120s (black solid line); bwGO (wine solid line); and the nanohybrids before incubation (t = 0: GO120s + ANG, gray dashed line; bwGO+ANG, orange dashed line); and after overnight incubation and purification (t = 13 h: GO120s@ANG, solid grey line; bwGO@ANG, solid orange line).

The UV-visible spectrum of ANGAF488 showed the presence of an absorption band at 495 nm due to the absorbance of the Alexa Fluor fluorophore, confirming that the functionalization of the covalent dye of the protein proceeded successfully. As for bwGO and GO120s samples, the UV-vis spectra showed a significant difference in the band attributed to π-π^* electronic transitions at the C–C bonds of the aromatic rings [46], which displayed a wavelength of maximum absorption at 240 nm and 230 nm, respectively. Furthermore, the shoulder located at 300 nm, and related to the n-π^* transition of the

C–O bond, was broadened and less evident for the bwGO sample than for the sample GO120s [20].

Regarding the hybrid GO and ANG mixed materials, the absorption band of Alexa Fluor 488 green fluorescent dye, with a maximum at the wavelength of 495 nm, was visible immediately after protein addition (t = 0) and in GO120s@ANG and bwGO@ANG samples, i.e., the pellets collected after overnight incubation (t = 13 h) and purification by centrifugation, with a bathochromic shift in the dye absorption band of approximately 5 nm.

Figure 2 displays the emission spectra for the free ANGAF488 and the protein just added to GOs (no incubation) or after overnight incubation, both before (Figure 2a) and after purification by two centrifugation steps with washing in between them (Figure 2b).

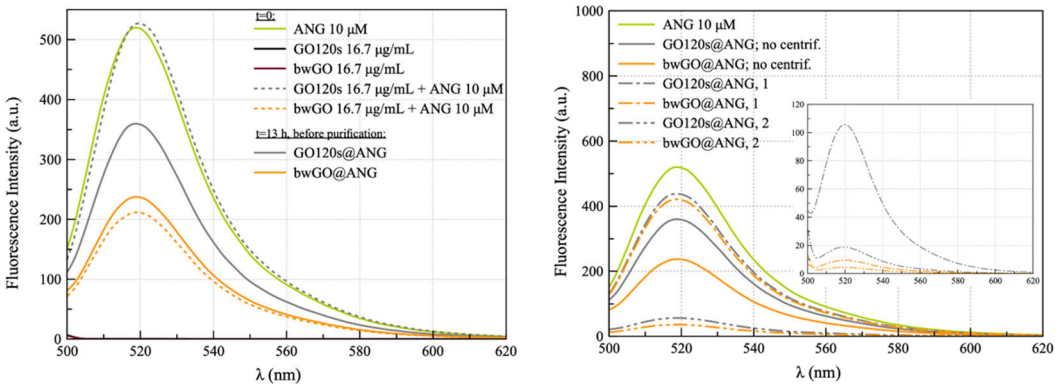

Figure 2. Emission spectra (λ_{ex} = 488 nm) for (**a**) ANGAF488 (10 μM), GO120s and bwGO sheets (16.7 μg/mL GO), the hybrids immediately after the addition of the protein to the GOs (GO + ANG, t = 0, dashed lines) and after overnight incubation, before purification (GO@ANG, t = 13 h, solid lines); (**b**) nanohybrids GO@ANG before purification and supernatants collected after the two steps of centrifugation (the correspondent pellets are reported in the inset).

Significant differences between the GOs upon interaction with the dye-labeled ANG were detected. Specifically, immediately after the addition of the protein (t = 0), the strong emission band of Alexa Fluor fluorophore, with a maximum at the wavelength of 519 nm, decreased approximately 40% from its original intensity value for bwGO+ANG, while remaining almost unchanged for GO120s + ANG. After overnight incubation (t = 13 h), the original dye emission was still quenched at about 60% for bwGO@ANG, but a noticeable decrease of about 30% in the fluorescence of the dye-labeled ANG was detected for GO120s@ANG.

2.2. Interaction of GO@ANG Hybrids with Prostate Cancer Cells: Cytotoxicity and Perturbation of Mitochondria and Cell Cytoskeleton

The results of the MTT assay in Figure 3 showed a statistically significant decrease in cell viability only for cells incubated 24 h with 0.55 μg/mL GO120s (about 18% less viable cells than the untreated control, $p < 0.05$), 2.78 μg/mL GO120s (about 14% less viable cells than the untreated control, $p < 0.05$) or 2.78 μg/mL bwGO (about 9% less viable cells than the untreated control, $p < 0.05$). Parallel experiments carried out in the presence of a copper-supplemented medium (100 nM or 500 nM, concentration equimolar to ANG), indicated similar results.

LSM live cell imaging was carried out to assess the different internalization pathways, if any, for the free dye-labeled ANGAF488 and the protein immobilized in the two GOs, either in the absence or presence of copper ions (Figure 4). To map the protein and GO nanosheets' intracellular localization, the PC-3 cells were stained at once at the nuclei and the mitochondria organelles.

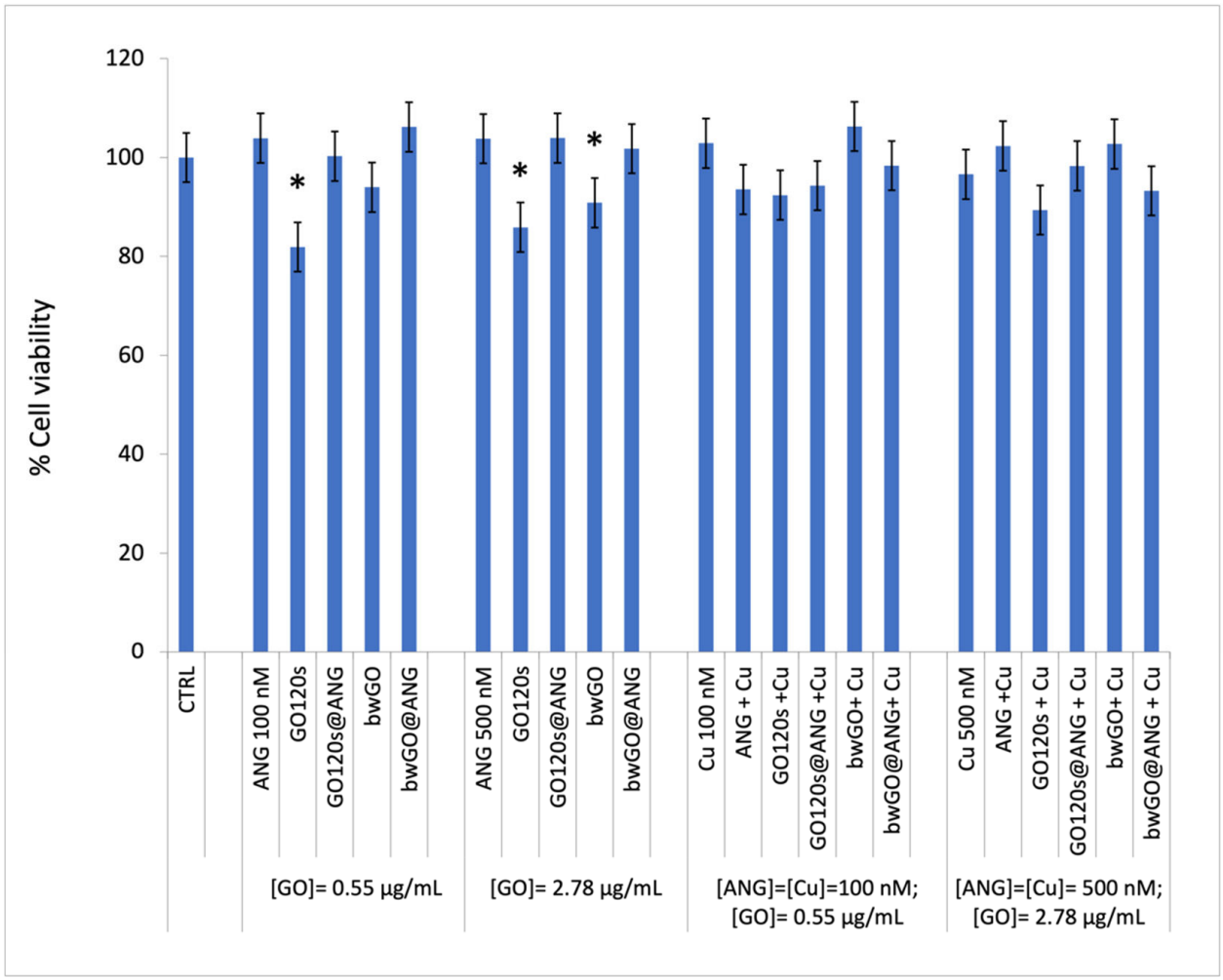

Figure 3. Cell viability of PC-3 cells after 24 h of treatment with the ANGAF488 protein (100 and 500 nM), GO120s or bwGO (0.55 and 2.78 µg/mL) and the corresponding GO@ANG nanohybrids, in the absence or presence of $CuSO_4$-supplemented medium (copper concentrations of 100 and 500 nM, with metal/protein molar ratio = 1). (*) $p < 0.05$, vs. CTRL. (Student's *t*-test).

From the bright field images, the GO sheets were recognizable in the cytoplasm for both GO120s (Figure 4b) and bwGO (Figure 4c) as polygonal black features (see white arrows) that destroyed the dense mitochondrial organelle distribution, pointed out by the red staining, which was instead observed in the control untreated cells (Figure 4a).

As for the protein internalized by the PC-3 cells, different distributions of the green fluorescence by the Alexa Fluor-labelled ANG were observed, in the absence of copper ions (Figure 4d–f), for the cells treated with the free ANGAF488 protein or the protein-immobilized GO120s and bwGO sheets. Specifically, the free protein mainly accumulated on the periphery of the cell membrane, with few yellow spots detected in the cytoplasm and the perinuclear region (Figure 4d; see yellow arrow). In contrast, GO120 sheets covered by the green fluorescent dye-labeled protein were fully internalized and visible in the cytoplasm (Figure 4e), while for cells incubated with bwGO@ANG, both protein accumulation in the cell membrane and polygonal green fluorescent characteristics inside the cell were found (Figure 4f).

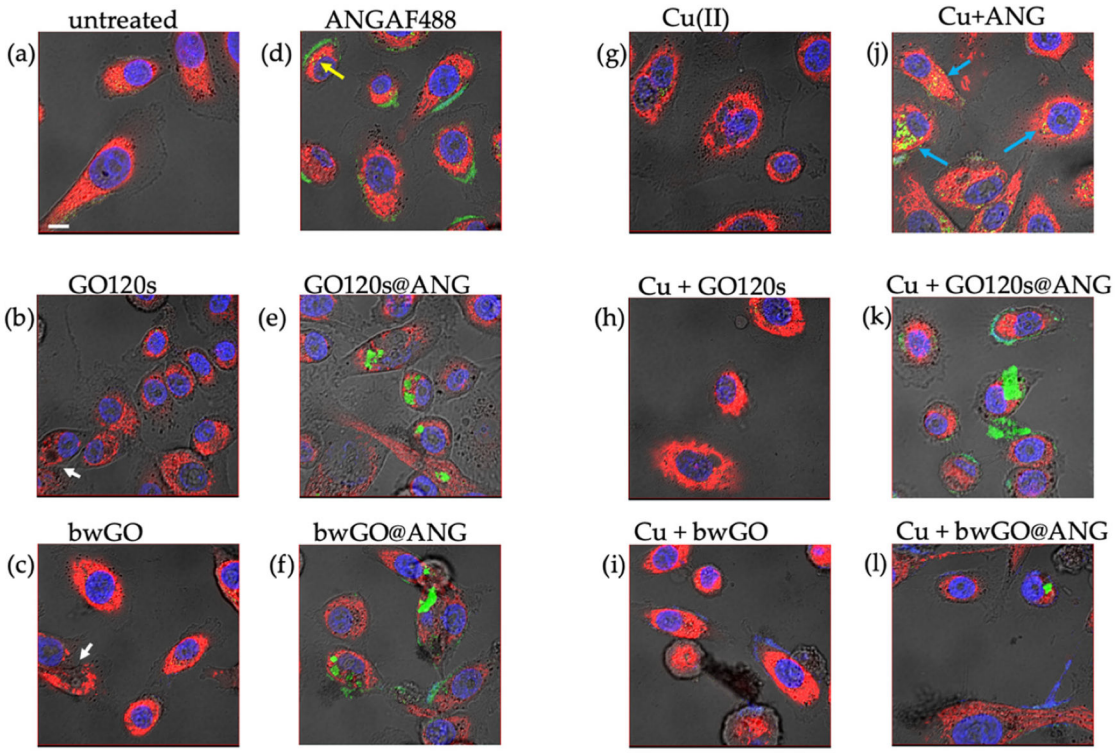

Figure 4. LSM-merged micrographs of optical bright field (in grey) and fluorescence (in blue: nuclear staining, Hoechst, λex/em = 405/425–450 nm; in red: mitochondrial staining, MitoTracker Deep Red, λex/em = 633/650–655 nm; in green: ANGAF488, Alexa Fluor, λex/em = 488/500–530 nm) recorded in live cell imaging of PC-3 cells untreated ((**a**): CTRL) and after 24 h of treatment with: 2.78 μg/mL GO120s (**b**) or bwGO (**c**); 500 nM AngAF488 (**d**); the hybrids (2.78 μg/mL in GO and 500 nM ANG) of GO120s@ANGF488 (**e**) or bwGO@ANGF488 (**f**); 500 nM $CuSO_4$ (**g**); 500 nM Cu-supplemented medium with 2.78 μg/mL of GO120s (**h**) or bwGO (**i**); 500 nM Cu-supplemented medium with ANGAF488 (**j**) or hybrids (2.78 μg/mL in GO and 500 nM ANG) of GO120s@ANGF488 (**k**) and bwGO@ANGF488 (**l**). Scale bar = 10 μm.

Regarding protein uptake by cells in copper-supplemented medium (Figure 4j–l), for the free protein, green fluorescence was observed mostly as sparse bright spots in the cytoplasm rather than at the cell membrane (Figure 4j, blue arrows), suggesting an active role of the metal in intracellular protein mobilization, likely due to its high affinity for bonding to ANG [37].

The mitochondrial staining allowed for discriminating perturbation on these organelles, induced by the different treatments. In terms of the negative control (untreated cells, Figure 4a), mitochondria exhibited a rather dense distribution and showed a characteristic ellipsoidal shape. A significant reduction in the red fluorescence signal was shown after the treatment with GO120s (Figure 4b) or with the hybrids GO@ANG, both in the absence (Figure 4e,f) or presence (Figure 4k,l) of copper.

The actin staining shown in Figure 5 confirmed the activity of the protein to bind to actin, leading to a marked reorganization of the cell cytoskeleton, with thick actin filaments, confined mainly along the cellular membrane, observed after the cell treatment with ANG (Figure 5b), copper (Figure 5g), or the protein-metal complex (Figure 5j) [47]. Thinner actin filaments were generally observed after treatment, in the absence or presence of copper-supplemented medium, with GO120 (Figure 5b,h) and bwGO (Figure 5c,i). This effect was amplified for the corresponding hybrids with the protein (Figure 5e,f,k,l), which indicates that interacting with F-actin decreases its assembly, thus impairing the cell cytoskeleton.

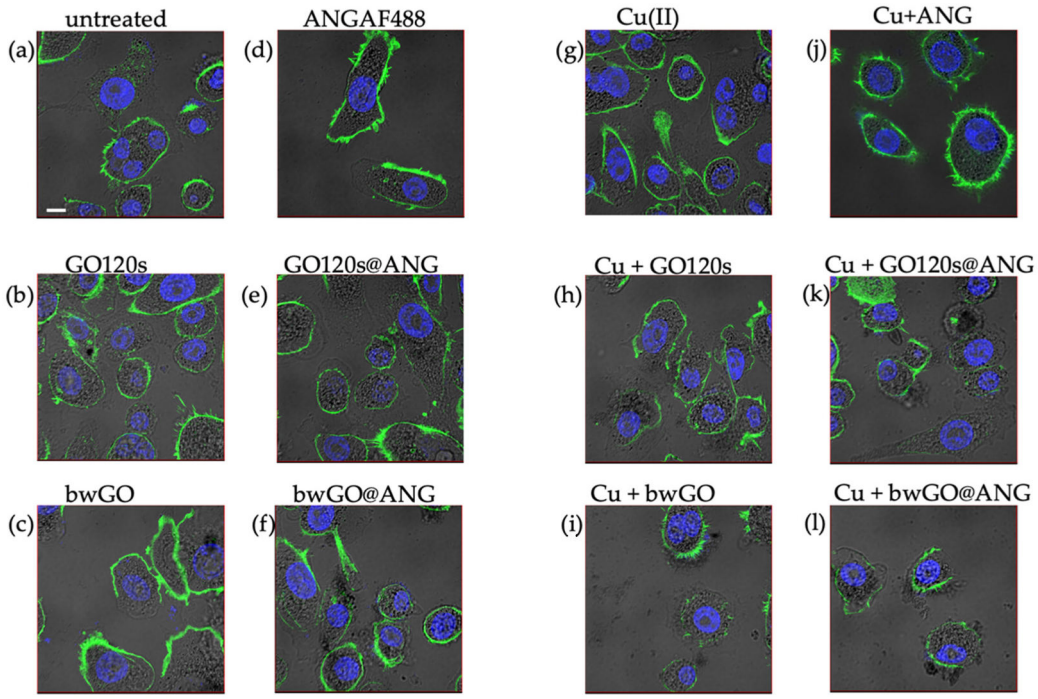

Figure 5. LSM-merged micrographs of optical bright field (in grey) and fluorescence (in blue: nuclear staining, Hoechst, λex/em = 405/425–450 nm; in green: cytoskeleton actin, Actin Green, λex/em = 488/500–530 nm) of PC-3 cells untreated ((**a**): CTRL) and after 24 h of treatment with: 2.78 μg/mL GO120s (**b**) or bwGO (**c**); 500 nM AngAF488 (**d**); the hybrids (2.78 μg/mL in GO and 500 nM ANG) of GO120s@ANGF488 (**e**) or bwGO@ANGF488 (**f**); 500 nM $CuSO_4$ (**g**); 500 nM Cu supplemented medium with 2.78 μg/mL of GO120s (**h**) or bwGO (**i**); 500 nM Cu supplemented medium with ANGAF488 (**j**) or hybrids (2.78 μg/mL in GO and 500 nM ANG) of GO120s@ANGF488 (**k**) and bwGO@ANGF488 (**l**). Scale bar = 10 μm.

3. Discussion

In the present work, bioconjugates were prepared by labeling the protein with the fluorophore Alexa fluor 488, which made the complex detectable by LSM. Although localization strategies that do not require labeling exist, e.g., using label-free confocal Raman imaging [48], our approach allowed us to scrutinize the hybrid nano-biointerface between the dye-labeled protein and the GO in terms of energy transfer processes, as discussed below.

The change of the UV-vis absorption relative intensity of the two transitions between GO120s and bwGO (Figure 1) can be explained by the reduced conjugative effect of the chromophores, as bwGO was treated to remove the strongly oxidated ODs, so reducing the average number of oxygen-containing functional groups conjugated with the sp^2 clusters [49]. In terms of GO sheets functionalized with ANG, although the GO absorption bands were covered by the background absorption of the fluorophore, markers of interaction between the nanosheets and the protein could still be detected in the UV-visible spectra. Fluorescence quenching is a valuable tool to study many macromolecular assemblies (Figure 2). It is well known that graphitic systems such as GO and rGO can strongly quench the emission of dye molecules through energy-transfer processes [50]. Note that the purification procedure was effective in removing the unbound or loosely bound protein molecules from the surface of the GO sheets (see spectra of the supernatants collected after the two centrifugation steps in Figure 2b). Moreover, notwithstanding the strong quenching of the dye expected for the protein molecules in close contact to the GOs, there was still a significant emission signal detected in the pellet samples (Figure 2b, inset), which indicated the successful immobilization of ANG adlayers, firmly attached to both GO120s and bwGO sheets in the hybrid GO@ANG samples.

The cellular toxicity of graphene depends on various possible mechanisms. In vitro studies of graphene have reported that the main causes of nanosheet cytotoxicity are physical interactions with cell membranes that lead to loss of cell integrity [51]. A more hydrophobic form of graphene shows high affinity for membrane lipids, while more hydrophilic sheets can bind to cell receptors, interfering with cell metabolism and nutrient supply, thus further inducing stress or cell death [52]. Furthermore, GO induces excessive ROS generation leading to damage to proteins, DNA, and lipids, influencing cell metabolism and signaling, and also inducing cellular aging and mutagenesis [53]. In addition, graphene can bind to micronutrients and amino acids present in the cell culture medium limiting their availability and inhibiting cellular growth and viability [54]. Our cell viability results (Figure 3) were in agreement with data from the literature that demonstrate a cell-dependent cytotoxicity with a predominant toxic effect of graphene and GO sheets on neuronal tumor cells (e.g., neuroblastoma, glioblastoma), liver cancer cells (HepG2), and lung cancer cells (A549). However, only a slight decrease in cell viability is observed with the improved influence of graphene on cell proliferation and survival in a human colorectal adenocarcinoma cell line (CaCo2) and prostate cancer cells (PC-3) [55]. In particular, it is found that after exposure to 20 μg/mL of graphene and GO, almost 90% of cancer cells remain viable [56]. Moreover, it is well known that the functionalization of graphene through covalent or non-covalent interaction by various materials, such as polymers, DNA and proteins, greatly improves the biocompatibility of nanosheets, enhancing its solubility, and significantly reduces its toxic interactions with living systems [57]. Also, metal ions can interact with the GO surface owing to the presence of carboxylic acid groups that can chelate copper ions, forming a complex system. Such a complex system is analogous to a copper compound, but with an expanded planar ligand and a size ranging from a few to hundreds of nanometers [58]. Accordingly, no reduction in PC-3 viability is observed for the surface-decorated GO120s and bwGO sheets.

Confocal microscopy imaging on PC-3 cells upon treatment with the different samples reveals a specific interaction of ANGF488 with the cell membrane and the actin cytoskeleton. It is known that ANG, through the amino acid sequence encompassing the residues from 60 to 68, which is also part of the cell-surface receptor binding site, makes a complex with the cell surface α-actin. The α-actin binding is a crucial step in the promotion of angiogenesis, since this complex can activate the plasminogen activator/plasmin serine protease system that leads to plasmin generation [59,60]. Furthermore, after interaction with actin, ANG induces changes in the cell cytoskeleton by inhibiting the polymerization of G-actin and changing the physical properties of F-actin, respectively [61]. These events severely alter the cell's mechanical properties, inducing strong effects on the cellular structure and function, and tissue morphogenesis, as well as on the whole angiogenic process [62,63]. In the presence of copper, a more diffuse localization of the protein in the cytoplasm is observed. Copper is an essential element in both humans and animals and is crucial to the health of living organisms. It has been recognized as an angiogenic factor capable of stimulating endothelial cell migration and neovascularization [64], while its depletion by Cu chelators, in vivo, prevents vessel formation [43,65].

Such an intersection between copper and angiogenesis supports the critical role of the metal in pathological and physiological angiogenic processes, such as cancer [66]. Moreover, it has been found that Cu binds to angiogenin. Human ANG shows glutamine, as the first residue, which spontaneously cyclized to a pyroglutamate ring. Such a structure allows the protein to make a complex with copper ions with a 1:1 metal-to-ligand stoichiometry at physiological pH and a ligand field that most likely involves two imidazole nitrogen atoms, one deprotonated nitrogen, and one oxygen atom [39]. The interaction between copper and ANG modulates the angiogenic response and the biological function of ANG, decreasing both the ribonucleolytic activity of the protein and its nuclear translocation, accordingly to our results [37]. As for the hybrid, there was a higher ability of GO120s to bind and traffic ANGF488 inside the cells, most likely due to the higher presence of reactive COOH and OH groups that facilitate connection with the protein.

4. Materials and Methods

4.1. Chemicals

Graphene oxide (chemically exfoliated) in an aqueous dispersion (0.4 wt.%) was purchased from Graphenea Inc.; US. Sodium hydroxide (NaOH, ≥97%, pellet) and hydrochloric acid (HCl, 37% in H_2O) were purchased from Sigma-Aldrich (St. Louis, MO, USA). The 3-(N-morpholino)-propane sulfonic acid (MOPS) buffer solution (added with 0.003 M KCl and 0.14 M NaCl) was prepared at a concentration of 1 mM and the pH was corrected to 7.4 (VWR, Radnor PA, USA). For all experiments, ultrapure water (18.2 mΩ·cm at 25 °C, total organic carbon (TOC) less than 5 parts per billion (ppb), UltrapureMillipore® Water Type) was used, and the glassware was cleaned with aqua regia (HCl:HNO_3 1:3 volume ratio) and rinsed with ultrapure water before each use. For all cellular experiments, RPMI-1640 medium, penicillin-streptomycin, L-glutamine, fetal bovine serum (FBS), dimethyl sulfoxide (DMSO), Dulbecco's phosphate-buffered saline (PBS), paraformaldehyde and 3-(4,5-dimethylthiazol-2-yl)-2,5-diphenyltetrazolium bromide (MTT) were purchased by Sigma-Aldrich.

4.2. Preparation of bwGO and GO120s

Base-washed GO was prepared by stripping the ODs from as-received GO aqueous dispersion following the procedure described by Thomas et al. [29]. Briefly, as-received GO was diluted with ultrapure water to a concentration of 0.56 mg / ml and then NaOH 1.32 M was added to GO at a final concentration of 14 mM. The alkaline solution was heated at 70 °C for 1 h under stirring and then centrifuged (30 min, 12500 r.p.m., RT). The pellet was collected and resuspended in ultrapure water, and another centrifugation step was performed. After treatment with NaOH, the dispersion was reprotonated by adding 14 mM HCl to neutralize the base previously employed. The same procedure described above for alkaline washing was applied. Eventually, the GO dispersion was ultrasonicated for 120 min utilizing a Hielscher UP50H ultrasonic processor (Amplitude 40%, Cycle 1) and the smaller nanosheets were collected by centrifugation (20 min, 13,000 rpm, RT) and collection of the supernatant.

GO 120s samples were prepared by ultra-sonication of the 0.56 mg/mL as-received GO aqueous dispersion for 120 min with a Hielscher UP50H ultrasonic processor (Amplitude 40%, Cycle 1). Afterward, the GO was centrifuged (20 min, 13,000 rpm, RT) and the supernatant was collected. Both bwGO and GO 120s supernatants were lyophilized overnight to provide the respective powder samples.

4.3. Angiogenin Expression, Purification and Fluorescent Labeling

The human ANG expression in the bacterial vector was performed following a previously reported method [67,68]. Briefly, cells of E. Coli (BL21(DE3) strain) cells were cultured at 37 °C shaking (180 r.p.m.) in terrific broth supplemented with ampicillin (100 μg/mL). After 24 h, cells were inoculated in 1 L of fresh broth and ANG expression was induced by the addition of 1 mM isopropyl β-D-1-thiogalactopyranoside (IPTG). Afterward, cells were harvested by centrifugation (4000 RCF for 15 min at 4 °C, JLA 8100) and lysed into 30 mL of lysis buffer (50 mM Tris-HCl, 2 mM EDTA, pH = 8) and using the high-pressure homogenizer (Emulsiflex) and sonicator (Qsonica Sonicator Q700).

The lysate was then centrifuged (20,000 RCF for 40 min at 4 °C, JA25.50) and resuspended in lysis buffer supplemented with 1% (*v*/*v*) Triton X-100, twice. The final pellet was dissolved in guanidine denaturation buffer. The expressed recombinant angiogenin (rANG) was refolded from inclusion bodies in agreement with the method reported by Jang et al. (2004) [69] and then purified utilizing cation-exchange chromatography performed on an automated chromatographic workstation (Akta prime, GE Healthcare) equipped with a 15 × 1.6 cm column packed with SP Sepharose Fast Flow (GE Healthcare). After a washing step with 25 mM Tris-HCl (pH = 8.0), rANG was eluted with 25 mM Tris-HCl, 1 M NaCl buffer solution (pH = 8.0) buffer solution. Human angiogenin (ANG) was obtained by specific removal of the N-terminal methionine residue of the protein using 1 nM Aeromonas

aminopeptidase, at a concentration of 1×10^{-5} M in 200 mM potassium phosphate buffer (pH = 7.2). Finally, ANG was purified by dialysis (Spectra/por MWCO 6–8000 Da), which replaces PBS with a buffer solution of 25 mM Tris-HCl (pH 7.4) buffer solution, followed by cation exchange chromatography.

The fluorescent derivative of ANG, namely ANGF488, was obtained by conjugating the primary amines (e.g., lysine residues) of the protein with the reactive dye of Alexa fluor 488 tetrafluorphenyl ester (TFP) (MW = 885 Da, ε = 71,000 $cm^{-1}M^{-1}$, λex/em = 494/519 nm) according to the manufacturer's protocol. Briefly, 50 µL of 1 M bicarbonate was added to 0.5 mL of 2 mg/mL ANG in 10 mM PBS. The protein solution was transferred to the vial containing the reactive dye, and the reaction mixture was incubated under stirring for 1 h at room temperature. Afterward, the mixture was loaded on a PD-10 desalting column (GE Healthcare) to separate the fluorescent protein from the free dye molecules. Following the protocol, as soon as the sample was included in the column gel, 3.5 mL of elution buffer (10 mM PBS, pH 7.4) was gently added to the column. The flow-through containing the fluorescent wtANG488F protein was collected and then concentrated employing Vivaspin tubes (MWCO 5000). The absorbance of the fluorescent conjugate solution at 280 nm and 494 nm was measured using a PerkinElmer spectrophotometer and quantified by the molar extinction coefficient. The recovery of the protein was around 80%, and the calculated degree of labeling (DOL), which corresponds to the average number of dye molecules coupled to the protein calculated according to the instruction provided by the kit, was 0.68. The concentrated protein was finally stored, after freezing with N_2 liquid, at −20 °C.

4.4. Synthesis of ANGF488-GO Hybrids

The synthesis of bwGO@ANGF488 and GO120s@ANGF488 hybrids in MOPS was performed by utilizing a one-pot functionalization procedure. A 10 mM MOPS solution was obtained by dissolving 0.418 g of MOPS salt, 0.040 g of KCl, and 1.6 g of NaCl in 200 mL of ultrapure water, and then adjusting the pH to 7.4. The GO 120s and bwGO powder were first suspended at a concentration of 0.1 mg/mL in MOPS 1 mM, then sonicated for 3 h to get stable colloidal solutions. To fabricate the nanohybrid platforms, the GO 120 s and bwGO solutions were brought to a concentration of 16.7 µg/mL in MOPS 1 mM and incubated for 13 h (37 °C, 400 rpm) in presence of 100 nM ANGF488. After the incubation period, both solutions were washed to remove the excessive ANG by two centrifugation steps (13,000 rpm, 20 min, RT) and 200 µL pellets for each nanohybrid solution were collected.

4.5. UV-Vis and Fluorescence Spectroscopies

The UV-vis analysis was performed on a Perkin-Elmer 365 spectrometer, using quartz cuvettes with an optical length of 1 cm and 0.1 cm. Fluorescence spectra were recorded using a Perkin-Elmer LS55 fluorimeter and quartz cuvettes with an optical path length of 0.1 cm.

4.6. Maintenance and Treatment of Cell Cultures

Prostate cancer cells (PC-3 line) were cultured in 25 cm^2 plastic flasks using RPMI-1640 medium supplemented with 10% (*v*/*v*) fetal bovine serum (FBS), and contained 2 mM L-glutamine, 100 UI penicillin/ 0.1 mg/mL streptomycin. Cells were grown in an incubator (Heraeus Hera Cell 150C incubator), under a humidified atmosphere at 37 °C in 5% CO_2. For the treatments, cells were incubated for 24 h in a medium supplemented with 1% (*v*/*v*) FBS with bwGO and GO120s at two concentrations (0.55 and 2.78 µg/mL); the bwGO@ANG and GO120s@ANG (ANG concentrations of 100 nM and 500 nM for GO concentrations of 0.55 µg/mL and 2.78 µg/mL, respectively) both in the absence and in presence of $CuSO_4$, at a metal/protein molar ratio of 1.

4.7. Cytotoxicity Assays

The cells were seeded in a 96-multiwell plate in a complete medium at a density of 15×10^3 cells per well. Afterward, cells were incubated in a medium supplemented with 1% (*v*/*v*) FBS for 24 h with the different samples. Cytotoxicity was determined by incubating the cells, at 37 °C, with the tetrazolium salt, 3-(4-dimethylthiazol-2-yl)-2,5-diphenyltetrazolium bromide (MTT), for 60 min. Subsequently, the enzymatic reduction of MTT to the insoluble purple formazan product was detected by dissolving the crystal with 100 µL of DMSO and measuring the absorbance at 570 nm using a Varioscan spectrophotometer (Varioskan® Flash Spectral Scanning Multimode Readers, Thermo Scientific). The experiments were carried out in triplicate and the results are presented as the means ± standard deviation (SD). The statistical analysis was performed by Student's *t*-test.

4.8. Confocal Microscopy Analysis

PC-3 cells were seeded in glass bottom plates (WillCo-dish®, Willco Wells, B.V.) with 12 mm glass diameter at a density of 25×10^3 cells per plate in full medium. Subsequently, cells were incubated for 24 h with the different samples. The cells were then stained with the nuclear dye Hoechst33342 (1 µg/mL) and MitoTracker deep red (2×10^{-7} M) before performing the 'live' cell imaging. Finally, cells were fixed with high-purity 2% paraformaldehyde in PBS, pH = 7.3, permeabilized with 0.5% (*v*/*v*) Triton X-100 supplemented with 0.1% (*w*/*v*) BSA in PBS, and then stained with a high-affinity F-actin probe, conjugated to green-fluorescent Alexa Fluor 488 dye (2 drops/mL) (Thermo Fisher Scientific).

Confocal microscopy studies were executed with an Olympus FV1000 confocal laser scanning microscope (LSM), equipped with diode UV (405 nm, 50 mW), multiline Argon (457 nm, 488 nm, 515 nm, total 30 mW), HeNe(G) (543 nm, 1 mW) and HeNe(R) (633 nm, 1 mW) lasers. An oil immersion objective (60xO PLAPO) and spectral filtering systems were used. The detector gain was fixed at a constant value, and images were collected, in sequential mode, randomly all through the area of the well. The image analysis was carried out using Huygens Essential software (by Scientific Volume Imaging B.V., The Netherlands). The statistical analysis was performed by Student's *t*-test.

Author Contributions: Conceptualization, C.S. and D.L.M.; methodology, T.M. and Ö.H.; investigation, L.R. and L.M.C.; writing: original draft preparation, L.R. and L.M.C.; writing: review and editing, C.S. and D.L.M. All authors have read and agreed to the published version of the manuscript.

Funding: This research was funded by MUR (PRIN), grant number 2017WBZFH, and the University of Catania (PIAno di inCEntivi per la RIcerca di Ateneo 2020/2022 CHANCE_Linea di Intervento 1 and GRABIO_Linea di intervento 2).

Data Availability Statement: Not applicable.

Conflicts of Interest: The authors declare no conflict of interest. The funders had no role in the design of the study; in the collection, analyses, or interpretation of data; in the writing of the manuscript; or in the decision to publish the results.

References

1. Carmeliet, P.; Jain, R.K. Molecular mechanisms and clinical applications of angiogenesis. *Nature* **2011**, *473*, 298–307. [CrossRef] [PubMed]
2. Darweesh, R.S.; Ayoub, N.M.; Nazzal, S. Gold nanoparticles and angiogenesis: Molecular mechanisms and biomedical applications. *Int. J. Nanomed.* **2019**, *14*, 7643–7663. [CrossRef] [PubMed]
3. Di Pietro, P.; Strano, G.; Zuccarello, L.; Satriano, C. Gold and Silver Nanoparticles for Applications in Theranostics. *Curr. Top. Med. Chem.* **2016**, *16*, 3069–3102. [CrossRef] [PubMed]
4. Li, M.; Wei, J.; Song, Y.; Chen, F. Gold nanocrystals: Optical properties, fine-tuning of the shape, and biomedical applications. *RSC Adv.* **2022**, *12*, 23057–23073. [CrossRef] [PubMed]
5. Song, J.; Wang, X.; Chang, C.-T. Preparation and Characterization of Graphene Oxide. *J. Nanomater.* **2014**, *2014*, 276143. [CrossRef]
6. Poyyakkara, A.; Thekkeveedu, S.; Shankar, S.; Sameer Kumar, V.B. Regulation of Angiogenesis Using Nanomaterial Based Formulations: An Emerging Therapeutic Strategy to Manage Multiple Pathological Conditions. In *Theranostics—An Old Concept in New Clothing*; IntechOpen: London, UK, 2020.

7. Cucci, L.M.; Trapani, G.; Hansson, Ö.; La Mendola, D.; Satriano, C. Gold Nanoparticles Functionalized with Angiogenin for Wound Care Application. *Nanomaterials* **2021**, *11*, 201. [CrossRef]
8. Di Pietro, P.; Zaccaro, L.; Comegna, D.; Del Gatto, A.; Saviano, M.; Snyders, R.; Cossement, D.; Satriano, C.; Rizzarelli, E. Silver nanoparticles functionalized with a fluorescent cyclic RGD peptide: A versatile integrin targeting platform for cells and bacteria. *RSC Adv.* **2016**, *6*, 112381–112392. [CrossRef]
9. Di Pietro, P.; Zimbone, S.; Grasso, G.; La Mendola, D.; Cossement, D.; Snyders, R.; Satriano, C. A Multifunctional Nanoplatform Made of Gold Nanoparticles and Peptides Mimicking the Vascular Endothelial Growth Factor. *Appl. Sci.* **2021**, *11*, 6333. [CrossRef]
10. Zhang, W.; Taheri-Ledari, R.; Ganjali, F.; Afruzi, F.H.; Hajizadeh, Z.; Saeidirad, M.; Qazi, F.S.; Kashtiaray, A.; Sehat, S.S.; Hamblin, M.R.; et al. Nanoscale bioconjugates: A review of the structural attributes of drug-loaded nanocarrier conjugates for selective cancer therapy. *Heliyon* **2022**, *8*, e09577. [CrossRef]
11. Halim, A.; Qu, K.-Y.; Zhang, X.-F.; Huang, N.-P. Recent Advances in the Application of Two-Dimensional Nanomaterials for Neural Tissue Engineering and Regeneration. *ACS Biomater. Sci. Eng.* **2021**, *7*, 3503–3529. [CrossRef]
12. Cui, L.; Liang, J.; Liu, H.; Zhang, K.; Li, J. Nanomaterials for Angiogenesis in Skin Tissue Engineering. *Tissue Eng. Part B Rev.* **2020**, *26*, 203–216. [CrossRef] [PubMed]
13. Mukherjee, S.; Sriram, P.; Barui, A.K.; Nethi, S.K.; Veeriah, V.; Chatterjee, S.; Suresh, K.I.; Patra, C.R. Graphene Oxides Show Angiogenic Properties. *Adv. Healthc. Mater.* **2015**, *4*, 1722–1732. [CrossRef] [PubMed]
14. Zare, P.; Aleemardani, M.; Seifalian, A.; Bagher, Z.; Seifalian, A.M. Graphene Oxide: Opportunities and Challenges in Biomedicine. *Nanomaterials* **2021**, *11*, 1083. [CrossRef] [PubMed]
15. Norahan, M.H.; Amroon, M.; Ghahremanzadeh, R.; Mahmoodi, M.; Baheiraei, N. Electroactive graphene oxide-incorporated collagen assisting vascularization for cardiac tissue engineering. *J. Biomed. Mater. Res. Part A* **2019**, *107*, 204–219. [CrossRef] [PubMed]
16. Qian, Y.; Song, J.; Zhao, X.; Chen, W.; Ouyang, Y.; Yuan, W.; Fan, C. 3D Fabrication with Integration Molding of a Graphene Oxide/Polycaprolactone Nanoscaffold for Neurite Regeneration and Angiogenesis. *Adv. Sci.* **2018**, *5*, 1700499. [CrossRef]
17. Rehman, S.R.u.; Augustine, R.; Zahid, A.A.; Ahmed, R.; Tariq, M.; Hasan, A. Reduced Graphene Oxide Incorporated GelMA Hydrogel Promotes Angiogenesis For Wound Healing Applications. *Int. J. Nanomed.* **2019**, *14*, 9603–9617. [CrossRef]
18. Barui, A.K.; Roy, A.; Das, S.; Bhamidipati, K.; Patra, C.R. Therapeutic Applications of Graphene Oxides in Angiogenesis and Cancers. In *Nanoparticles and their Biomedical Applications*; Springer: Singapore, 2020; pp. 147–189.
19. Bugárová, N.; Špitálsky, Z.; Mičušík, M.; Bodík, M.; Šiffalovič, P.; Koneracká, M.; Závišová, V.; Kubovčíková, M.; Kajanová, I.; Zaťovičová, M.; et al. A Multifunctional Graphene Oxide Platform for Targeting Cancer. *Cancers* **2019**, *11*, 753. [CrossRef]
20. Tomasella, P.; Sanfilippo, V.; Bonaccorso, C.; Cucci, L.M.; Consiglio, G.; Nicosia, A.; Mineo, P.G.; Forte, G.; Satriano, C. Theranostic Nanoplatforms of Thiolated Reduced Graphene Oxide Nanosheets and Gold Nanoparticles. *Appl. Sci.* **2020**, *10*, 5529. [CrossRef]
21. Trapani, G.; Caruso, V.C.L.; Cucci, L.M.; Attanasio, F.; Tabbì, G.; Forte, G.; La Mendola, D.; Satriano, C. Graphene Oxide Nanosheets Tailored With Aromatic Dipeptide Nanoassemblies for a Tuneable Interaction With Cell Membranes. *Front. Bioeng. Biotechnol.* **2020**, *8*, 427. [CrossRef]
22. Verde, V.; Longo, A.; Cucci, L.M.; Sanfilippo, V.; Magrì, A.; Satriano, C.; Anfuso, C.D.; Lupo, G.; La Mendola, D. Anti-Angiogenic and Anti-Proliferative Graphene Oxide Nanosheets for Tumor Cell Therapy. *Int. J. Mol. Sci.* **2020**, *21*, 5571. [CrossRef]
23. Zhang, Y.; Ali, S.F.; Dervishi, E.; Xu, Y.; Li, Z.; Casciano, D.; Biris, A.S. Cytotoxicity Effects of Graphene and Single-Wall Carbon Nanotubes in Neural Phaeochromocytoma-Derived PC12 Cells. *ACS Nano* **2010**, *4*, 3181–3186. [CrossRef] [PubMed]
24. Patra, C.R. Graphene oxides and the angiogenic process. *Nanomedicine* **2015**, *10*, 2959–2962. [CrossRef] [PubMed]
25. Tojo, T.; Ushio-Fukai, M.; Yamaoka-Tojo, M.; Ikeda, S.; Patrushev, N.; Alexander, R.W. Role of gp91 phox (Nox2)-Containing NAD(P)H Oxidase in Angiogenesis in Response to Hindlimb Ischemia. *Circulation* **2005**, *111*, 2347–2355. [CrossRef] [PubMed]
26. Jarosz, A.; Skoda, M.; Dudek, I.; Szukiewicz, D. Oxidative Stress and Mitochondrial Activation as the Main Mechanisms Underlying Graphene Toxicity against Human Cancer Cells. *Oxidative Med. Cell. Longev.* **2016**, *2016*, 5851035. [CrossRef] [PubMed]
27. Consiglio, G.; Di Pietro, P.; D'Urso, L.; Forte, G.; Grasso, G.; Sgarlata, C.; Cossement, D.; Snyders, R.; Satriano, C. Surface tailoring of polyacrylate-grafted graphene oxide for controlled interactions at the biointerface. *J. Colloid Interface Sci.* **2017**, *506*, 532–542. [CrossRef]
28. Faria, A.F.; Perreault, F.; Elimelech, M. Elucidating the Role of Oxidative Debris in the Antimicrobial Properties of Graphene Oxide. *ACS Appl. Nano Mater.* **2018**, *1*, 1164–1174. [CrossRef]
29. Thomas, H.R.; Day, S.P.; Woodruff, W.E.; Vallés, C.; Young, R.J.; Kinloch, I.A.; Morley, G.W.; Hanna, J.V.; Wilson, N.R.; Rourke, J.P. Deoxygenation of Graphene Oxide: Reduction or Cleaning? *Chem. Mater.* **2013**, *25*, 3580–3588. [CrossRef]
30. Ivanov, P.; O'Day, E.; Emara, M.M.; Wagner, G.; Lieberman, J.; Anderson, P. G-quadruplex structures contribute to the neuroprotective effects of angiogenin-induced tRNA fragments. *Proc. Natl. Acad. Sci. USA* **2014**, *111*, 18201–18206. [CrossRef]
31. Lee, S.H.; Kim, K.W.; Min, K.-M.; Kim, K.-W.; Chang, S.-I.; Kim, J.C. Angiogenin Reduces Immune Inflammation via Inhibition of TANK-Binding Kinase 1 Expression in Human Corneal Fibroblast Cells. *Mediat. Inflamm.* **2014**, *2014*, 861435. [CrossRef]
32. Eleftheriadis, T.; Pissas, G.; Sounidaki, M.; Antoniadis, N.; Antoniadi, G.; Liakopoulos, V.; Stefanidis, I. Angiogenin is upregulated during the alloreactive immune response and has no effect on the T-cell expansion phase, whereas it affects the contraction phase by inhibiting CD4+ T-cell apoptosis. *Exp. Ther. Med.* **2016**, *12*, 3471–3475. [CrossRef]

33. Hu, G.f.; Riordan, J.F.; Vallee, B.L. A putative angiogenin receptor in angiogenin-responsive human endothelial cells. *Proc. Natl. Acad. Sci. USA* **1997**, *94*, 2204–2209. [CrossRef] [PubMed]
34. Greenway, M.J.; Andersen, P.M.; Russ, C.; Ennis, S.; Cashman, S.; Donaghy, C.; Patterson, V.; Swingler, R.; Kieran, D.; Prehn, J.; et al. ANG mutations segregate with familial and 'sporadic' amyotrophic lateral sclerosis. *Nat. Genet.* **2006**, *38*, 411–413. [CrossRef] [PubMed]
35. Bradshaw, W.J.; Rehman, S.; Pham, T.T.K.; Thiyagarajan, N.; Lee, R.L.; Subramanian, V.; Acharya, K.R. Structural insights into human angiogenin variants implicated in Parkinson's disease and Amyotrophic Lateral Sclerosis. *Sci. Rep.* **2017**, *7*, srep41996. [CrossRef]
36. Yoshioka, N.; Wang, L.; Kishimoto, K.; Tsuji, T.; Hu, G.f. A therapeutic target for prostate cancer based on angiogenin-stimulated angiogenesis and cancer cell proliferation. *Proc. Natl. Acad. Sci. USA* **2006**, *103*, 14519–14524. [CrossRef] [PubMed]
37. Giacomelli, C.; Trincavelli, M.L.; Satriano, C.; Hansson, Ö.; La Mendola, D.; Rizzarelli, E.; Martini, C. Copper (II) ions modulate Angiogenin activity in human endothelial cells. *Int. J. Biochem. Cell Biol.* **2015**, *60*, 185–196. [CrossRef]
38. Cucci, L.M.; Satriano, C.; Marzo, T.; La Mendola, D. Angiogenin and Copper Crossing in Wound Healing. *Int. J. Mol. Sci.* **2021**, *22*, 10704. [CrossRef] [PubMed]
39. La Mendola, D.; Arnesano, F.; Hansson, Ö.; Giacomelli, C.; Calò, V.; Mangini, V.; Magrì, A.; Bellia, F.; Trincavelli, M.L.; Martini, C.; et al. Copper binding to naturally occurring, lactam form of angiogenin differs from that to recombinant protein, affecting their activity. *Metallomics* **2016**, *8*, 118–124. [CrossRef]
40. Badet, J.; Soncin, F.; Guitton, J.D.; Lamare, O.; Cartwright, T.; Barritault, D. Specific binding of angiogenin to calf pulmonary artery endothelial cells. *Proc. Natl. Acad. Sci. USA* **1989**, *86*, 8427–8431. [CrossRef]
41. Urso, E.; Maffia, M. Behind the Link between Copper and Angiogenesis: Established Mechanisms and an Overview on the Role of Vascular Copper Transport Systems. *J. Vasc. Res.* **2015**, *52*, 172–196. [CrossRef]
42. Nielsen, V.G.; Ward, T.D.; Ford, P.M. Effects of cupric chloride on coagulation in human plasma: Role of fibrinogen. *J. Thromb. Thrombolysis* **2018**, *46*, 359–364. [CrossRef]
43. McAuslan, B.R.; Reilly, W. Endothelial cell phagokinesis in response to specific metal ions. *Exp. Cell Res.* **1980**, *130*, 147–157. [CrossRef]
44. La Mendola, D.; Giacomelli, C.; Rizzarelli, E. Intracellular Bioinorganic Chemistry and Cross Talk Among Different -Omics. *Curr. Top. Med. Chem.* **2016**, *16*, 3103–3130. [CrossRef] [PubMed]
45. Venturelli, S.; Leischner, C.; Helling, T.; Renner, O.; Burkard, M.; Marongiu, L. Minerals and Cancer: Overview of the Possible Diagnostic Value. *Cancers* **2022**, *14*, 1256. [CrossRef]
46. Assunção, I.C.C.; Sério, S.; Ferreira, Q.; Jones, N.C.; Hoffmann, S.V.; Ribeiro, P.A.; Raposo, M. Graphene Oxide Layer-by-Layer Films for Sensors and Devices. *Nanomaterials* **2021**, *11*, 1556. [CrossRef] [PubMed]
47. Satriano, C.; Munzone, A.; Cucci, L.M.; Giacomelli, C.; Trincavelli, M.L.; Martini, C.; Rizzarelli, E.; La Mendola, D. Angiogenin-mimetic peptide functionalised gold nanoparticles for cancer therapy applications. *Microchem. J.* **2018**, *136*, 157–163. [CrossRef]
48. Eliášová Sohová, M.; Bodík, M.; Siffalovic, P.; Bugárová, N.; Labudová, M.; Zaťovičová, M.; Hianik, T.; Omastová, M.; Majková, E.; Jergel, M.; et al. Label-free tracking of nanosized graphene oxide cellular uptake by confocal Raman microscopy. *Analyst* **2018**, *143*, 3686–3692. [CrossRef]
49. Lai, Q.; Zhu, S.; Luo, X.; Zou, M.; Huang, S. Ultraviolet-visible spectroscopy of graphene oxides. *AIP Adv.* **2012**, *2*, 032146. [CrossRef]
50. Srivastava, S.; Senguttuvan, T.D.; Gupta, B.K. Highly efficient fluorescence quenching with chemically exfoliated reduced graphene oxide. *J. Vac. Sci. Technol. B* **2018**, *36*, 04G104. [CrossRef]
51. Seabra, A.B.; Paula, A.J.; de Lima, R.; Alves, O.L.; Durán, N. Nanotoxicity of Graphene and Graphene Oxide. *Chem. Res. Toxicol.* **2014**, *27*, 159–168. [CrossRef]
52. Jaworski, S.; Sawosz, E.; Grodzik, M.; Winnicka, A.; Prasek, M.; Wierzbicki, M.; Chwalibog, A. In vitro evaluation of the effects of graphene platelets on glioblastoma multiforme cells. *Int. J. Nanomed.* **2013**, *8*, 413–420. [CrossRef]
53. De Marzi, L.; Ottaviano, L.; Perrozzi, F.; Nardone, M.; Santucci, S.; De Lapuente, J.; Borras, M.; Treossi, E.; Palermo, V.; Poma, A. Flake size-dependent cyto and genotoxic evaluation of graphene oxide on in vitro A549, CaCo2 and vero cell lines. *J. Biol. Regul. Homeost. Agents* **2014**, *28*, 281–289. [PubMed]
54. Chng, E.L.K.; Sofer, Z.; Pumera, M. Cytotoxicity Profile of Highly Hydrogenated Graphene. *Chem.—Eur. J.* **2014**, *20*, 6366–6373. [CrossRef] [PubMed]
55. Wilson, M.; Warren, J.M.; Abbott, L. Infantile stimulation, activity, and learning by cats. *Child Dev.* **1965**, *36*, 843–853. [CrossRef] [PubMed]
56. Zhou, H.; Zhang, B.; Zheng, J.; Yu, M.; Zhou, T.; Zhao, K.; Jia, Y.; Gao, X.; Chen, C.; Wei, T. The inhibition of migration and invasion of cancer cells by graphene via the impairment of mitochondrial respiration. *Biomaterials* **2014**, *35*, 1597–1607. [CrossRef] [PubMed]
57. Kim, M.-G.; Park, J.; Shon, Y.; Shim, G.; Oh, Y.-K. Pharmaceutical Applications of Graphene-based Nanosheets. *Curr. Pharm. Biotechnol.* **2014**, *14*, 1016–1026. [CrossRef]
58. Ren, H.; Wang, C.; Zhang, J.; Zhou, X.; Xu, D.; Zheng, J.; Guo, S.; Zhang, J. DNA Cleavage System of Nanosized Graphene Oxide Sheets and Copper Ions. *ACS Nano* **2010**, *4*, 7169–7174. [CrossRef]

59. Hallahan, T.W.; Shapiro, R.; Vallee, B.L. Dual site model for the organogenic activity of angiogenin. *Proc. Natl. Acad. Sci. USA* **1991**, *88*, 2222–2226. [CrossRef]
60. Hu, G.F.; Riordan, J.F. Angiogenin Enhances Actin Acceleration of Plasminogen Activation. *Biochem. Biophys. Res. Commun.* **1993**, *197*, 682–687. [CrossRef]
61. Pyatibratov, M.G.; Kostyukova, A.S. New Insights into the Role of Angiogenin in Actin Polymerization. In *International Review of Cell and Molecular Biology*; Elsevier: Amsterdam, The Netherlands, 2012; pp. 175–198.
62. Janmey, P.A. The Cytoskeleton and Cell Signaling: Component Localization and Mechanical Coupling. *Physiol. Rev.* **1998**, *78*, 763–781. [CrossRef]
63. Ingber, D.E. Mechanical control of tissue morphogenesis during embryological development. *Int. J. Dev. Biol.* **2006**, *50*, 255–266. [CrossRef]
64. Raju, K.S.; Alessandri, G.; Ziche, M.; Gullino, P.M. Ceruloplasmin, copper ions, and angiogenesis. *J. Natl. Cancer Inst.* **1982**, *69*, 1183–1188. [PubMed]
65. Brem, S.; Tsanaclis, A.M.; Zagzag, D. Anticopper treatment inhibits pseudopodial protrusion and the invasive spread of 9L gliosarcoma cells in the rat brain. *Neurosurgery* **1990**, *26*, 391–396. [CrossRef]
66. Apelgot, S.; Coppey, J.; Fromentin, A.; Guille, E.; Poupon, M.F.; Roussel, A. Altered distribution of copper (64Cu) in tumor-bearing mice and rats. *Anticancer. Res.* **1986**, *6*, 159–164. [PubMed]
67. Holloway, D.E.; Hares, M.C.; Shapiro, R.; Subramanian, V.; Acharya, K.R. High-Level Expression of Three Members of the Murine Angiogenin Family in Escherichia coli and Purification of the Recombinant Proteins. *Protein Expr. Purif.* **2001**, *22*, 307–317. [CrossRef] [PubMed]
68. Naletova, I.; Cucci, L.M.; D'Angeli, F.; Anfuso, C.D.; Magrì, A.; La Mendola, D.; Lupo, G.; Satriano, C. A Tunable Nanoplatform of Nanogold Functionalised with Angiogenin Peptides for Anti-Angiogenic Therapy of Brain Tumours. *Cancers* **2019**, *11*, 1322. [CrossRef] [PubMed]
69. Jang, S.-H.; Kang, D.-K.; Chang, S.-I.; Scheraga, H.A.; Shin, H.-C. High level production of bovine angiogenin in E. coli by an efficient refolding procedure. *Biotechnol. Lett.* **2004**, *26*, 1501–1504. [CrossRef] [PubMed]